JFM RAPIDS
journals.cambridge.org/rapids

Revisiting inclination of large-scale motions in unstably stratified channel flow

Scott T. Salesky[1,†] **and W. Anderson**[2]

[1]School of Meteorology, The University of Oklahoma, Norman, OK 73072, USA

[2]Mechanical Engineering Department, The University of Texas at Dallas, Richardson, TX 75080, USA

Observational and computational studies of inertia-dominated wall turbulence with unstable thermal stratification have demonstrated that the inclination angle of large-scale motions (LSMs) increases with increasing buoyancy (as characterized by the Monin–Obukhov stability variable ζ_z). The physical implications of this structural steepening have received relatively less attention. Some authors have proposed that LSMs thicken – yet remain attached to the wall – with increasing buoyancy (Salesky & Anderson, *J. Fluid Mech.*, vol. 856, 2018, pp. 135–168), while others have presented evidence that the upstream edge of an LSM remains anchored to the wall while its downstream edge lifts away from the wall (Hommema & Adrian, *Boundary-Layer Meteorol.*, vol. 106, 2003, pp. 147–170). Using a suite of large-eddy simulations (LES) of unstably stratified turbulent channel flow, we demonstrate that buoyancy acts to lift LSMs away from the wall, leaving a wedge of fluid beneath with differing momentum. We develop a prognostic model for LSM inclination angle that accounts for this observed structure, where the LSM inclination angle γ is the sum of the inclination angle observed in a neutrally stratified wall-bounded turbulent flow, $\gamma_0 \approx 12°$–$15°$, and the stability-dependent inclination angle of the wedge $\gamma_w(\zeta_z)$. Reported values of $\gamma(\zeta_z)$ from the literature, LES results and atmospheric surface layer observations are found to be in good agreement with the new model for $\gamma(\zeta_z)$.

Key words: atmospheric flows, turbulent boundary layers, turbulent convection

1. Introduction

Large-scale motions (LSMs) – sinuous streaks meandering within the outer (inertial) layer of inertia-dominated wall turbulence – are responsible for turbulence production and locally enhanced surface fluxes (Hutchins & Marusic 2007; Marusic & Heuer 2007). The existence of LSMs is predicated upon inertial conditions, with

† Email address for correspondence: salesky@ou.edu

$Re_\tau = u_\tau \delta \nu^{-1} \gtrsim 2 \times 10^3$ a commonly cited metric, where u_τ, δ and ν represent the shear velocity scale, flow depth and kinematic viscosity, respectively. LSMs have received significant attention in flows sustained solely by mechanical shear (that is, neutrally stratified pipes, channels, and boundary layers), where they have been found to be inclined in the streamwise direction at angle $\gamma = \gamma_0 \approx 12°$–$15°$ (Carper & Porté-Agel 2004; Marusic & Heuer 2007; Chauhan *et al.* 2013). In the present article, we focus on the mean structure inclination angle, rather than that of individual flow structures; for discussion, see Deshpande, Monty & Marusic (2019).

In inertia-dominated wall turbulence with unstable thermal stratification, structure inclination angles increase (i.e. $\gamma > \gamma_0$) with increasing buoyancy forcing (Carper & Porté-Agel 2004; Marusic & Heuer 2007; Chauhan *et al.* 2013; Salesky & Anderson 2018), with LSMs eventually transitioning to vertical buoyant plumes when mechanical shear becomes negligible (Salesky, Chamecki & Bou-Zeid 2017; Salesky & Anderson 2018). However, changes in the morphology of LSMs with increasing thermal stratification, and how these morphological properties contribute to observed structure inclination angles, are not well understood. Salesky & Anderson (2018) explained observed changes in amplitude modulation with increasing thermal stratification by a conceptual model, whereby LSMs shorten and steepen – while remaining attached to the wall. However, smoke visualization experiments conducted by Hommema & Adrian (2003) in the neutral and unstable atmospheric surface layer suggest an alternative mechanism, where the neutrally stratified inclination angle is preserved, while the downstream edge of an LSM 'lifts up' from the wall due to buoyancy, leaving a wedge of high-momentum fluid beneath.

We investigate the effects of buoyancy on LSM structure – which is highly significant given the pivotal importance of LSMs in the description of wall turbulence across thermal regimes – using large-eddy simulation (LES) of channel flow subjected to mechanical shear and buoyancy under asymptotic-Re_τ conditions. Flow visualizations and conditional sampling reveal that the downstream edge of an LSM lifts up from the wall with increasingly unstable stratification, leaving a wedge of high-momentum fluid beneath, in agreement with the smoke visualization experiments of Hommema & Adrian (2003). A new model for LSM inclination angle that accounts for this observed structure is developed, where the inclination angle, $\gamma(\zeta_z)$, is the sum of γ_0 and the stability-dependent inclination angle of the high-momentum wedge, $\gamma_w(\zeta_z)$, beneath the LSM, where $\zeta_z = z/L$ is the Monin–Obukhov stability parameter and $L = -u_\tau^3 \Theta_0 / \kappa g Q_0$ is the Obukhov length, where Θ_0 is a reference potential temperature, g is acceleration due to gravity, κ is the von Kármán constant, and Q_0 is the kinematic surface heat flux. (In this article, vectors are denoted with the standard nomenclature, $\boldsymbol{x} = \{x, y, z\}$, where the first, second and third component corresponds with magnitude in the streamwise, spanwise and wall-normal direction, respectively). Thus, the morphology of LSMs can be viewed as remaining quasi-self-similar as buoyancy forcing increases. The neutral inclination angle γ_0 is preserved while buoyancy acts orthogonal to shear to lift the downstream edge of the LSM away from the wall, forming a wedge structure underneath.

This article is organized as follows. Results from LES modelling and a conceptual model for LSM steepening are presented in § 2. Details of specific cases and the LES numerical procedure can be found in the Appendix. A prognostic model that connects LSM steepening under unstable stratification to observed structure inclination angles is presented in § 3. To demonstrate efficacy of the model and LES results, a literature survey of existing γ values from experimental and field measurements is presented in § 4. Concluding remarks are presented in § 5. Throughout this article, wall turbulence

affected by thermal stratification will be characterized via the stability variables, $\zeta_z = z/L$ and $\zeta_\delta = \delta/L$ (the global stability variable based on the outer length scale), where z is distance from the wall. It follows that $\zeta_\delta < 0$, $\zeta_\delta = 0$ and $\zeta_\delta > 0$ correspond with unstable, neutral and stable stratification, respectively, while $\zeta_\delta \to -\infty$ and $\zeta_\delta \to \infty$ correspond with free convection and cessation of turbulence, respectively.

2. Large-scale motion inclination

We present results of LES modelling of turbulent channel flow subjected to unstable thermal stratification; we consider high-resolution LES, with case details summarized in table 1. The LES cases encompass a range of stratification conditions, from a quasi-neutral case ($-\zeta_\delta = 0.31$) to a case strongly influenced by buoyancy ($-\zeta_\delta = 266.5$). The cases and results have been carefully assembled to demonstrate changes in LSM structure across a wide range of stability conditions.

Figure 1 shows instantaneous streamwise–wall-normal plane flow visualization of streamwise velocity (a,d,g), vertical velocity (b,e,h) and potential temperature (c,f,i), for $-\zeta_\delta = 0.31$ (a–c), $-\zeta_\delta = 9.38$ (d–f) and $-\zeta_\delta = 266.5$ (g–i). On the panels, the interfaces of uniform momentum and temperature zones (UMZ, UTZ) are denoted by thin black lines, determined here via the fuzzy clustering method recently proposed by Fan *et al.* (2019). LSMs are visualized using three zones for vertical momentum and four zones for streamwise momentum and temperature, which provide a clear and objective indication of zone interfaces. We emphasize that the internal zones are presented for flow visualization purposes; examining statistical properties of uniform momentum/temperature zones is not the focus of this work. Heavy black lines on all panels denote inclination angles, $\gamma(\zeta_z)$, determined *a posteriori* from LES data, following the procedure presented in Chauhan *et al.* (2013), where the two-point correlation of streamwise velocity,

$$R_{uu}(\Delta x, \Delta z; \zeta_z) = \frac{\langle u(x, y, z, t)u(x + \Delta x, y, z + \Delta z, t)\rangle_{yt}}{\sigma_{u(x,y,z,t)}\sigma_{u(x+\Delta x,y,z+\Delta z,t)}}, \tag{2.1}$$

was calculated as a function of streamwise and vertical spatial lag (Δx and Δz); $\langle . \rangle_a$ denotes averaging computed over dimension a. The structure inclination angle was calculated as $\gamma = \tan^{-1}(\langle \Delta z / \Delta x^\star \rangle)$, where $\Delta x^\star$ is the streamwise lag corresponding to the maximum correlation. Dashed black lines in figure 1(d–i) denote the wedge inclination angle, calculated assuming a neutral inclination angle of $\gamma_0 = 12°$ (discussion to follow).

Figure 1(a–c), for which temperature is effectively a passive scalar, shows the 'standard' instantaneous realizations of inclined structures. Panel (a) reveals a series of inclined pools of relative-momentum deficit – confirmed by superposition of UMZ interfaces; these are generally observed to undergo a streamwise coalescence, forming so-called very-large-scale motions (VLSM) (Hutchins & Marusic 2007). There exists a predominant anticorrelation between the signs of $\tilde{u}'$ and $\tilde{w}'$, where low- and high-momentum regions (LMR, HMR) exhibit positive and negative vertical velocity, respectively. This is precisely seen on figure 1(b), where the figure 1(a) inclination lines encapsulate regions of uplift associated with net streamwise-momentum deficit. The implications of this for temperature – which, again, may be regarded as a passive quantity for the case of $-\zeta_\delta = 0.31$ (a–c) – are evident on (c). Plumes of positive vertical velocity within LMRs induce vertical transport of relative-temperature excess upwards, away from the wall, while zones of negative vertical velocity (b)
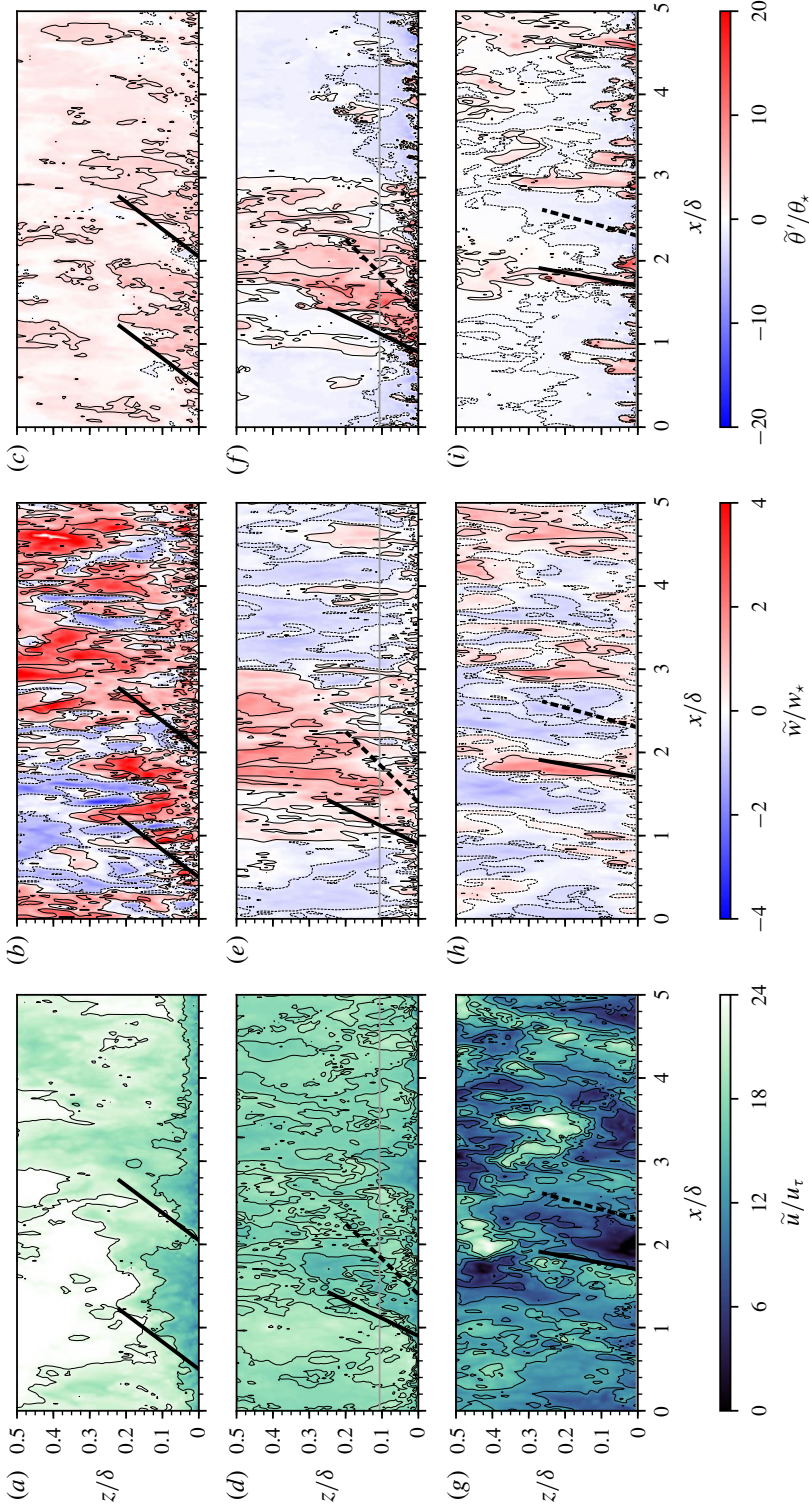
FIGURE 1. Instantaneous flow visualization of (a,d,g) streamwise velocity $\widetilde{u}/u_\tau$, (b,e,h) vertical velocity $\widetilde{w}/w_\star$ and (c,f,i) temperature fluctuations $\widetilde{\theta'}/\theta_\star$ (where $\theta_\star = Q_0/w_\star$ is the convective temperature scale) from LES in the x–z plane. Panels $(a$–$c)$ are displayed for $-\zeta_\delta = 0.31$, $(d$–$f)$ for $-\zeta_\delta = 9.38$ and $(g$–$i)$ for $-\zeta_\delta = 266.5$. Contour lines denote the interfaces of zones of uniform streamwise momentum (a,d,g), vertical momentum (b,e,h) and temperature fluctuations (c,f,i); thick black solid lines indicate the structure inclination angle $\gamma(\zeta_z)$ (equation (2.1) and accompanying text), thick black dashed lines indicate the wedge inclination angle $\gamma_w(\zeta_z)$ (discussed further in §3) and horizontal grey lines denote the Obukhov length $(-L/\delta)$.

transport relative-temperature deficit towards the wall. Larger values of $-\zeta_\delta$ alter LSMs dramatically, as large thermal gradients induce buoyant forces, enhancing vertical mixing.

For $-\zeta_\delta = 9.38$, figure 1(*d–f*) shows streamwise velocity, vertical velocity and temperature, respectively, for an arbitrarily selected instantaneous realization. Unlike for the quasi-neutral case (*a–c*), where LSMs remain 'anchored' to the wall, in (*d–f*) the downstream edge of selected LSMs shows a distinct uplift in the streamwise direction. This is consistent with the observations of Hommema & Adrian (2003), but contrary to the interpretation of a 'structural thickening' (Salesky & Anderson 2018). The region of streamwise-momentum deficit noted with solid inclination angle (*d*) resides above a region of streamwise-momentum excess – where inclination of the lower wedge is denoted by a heavy dashed black line. On (*e*), the standard $\tilde{u}'-\tilde{w}'$ anticorrelation is again clear – as per (*a*) and (*b*) – but now the region of collective positive $\tilde{w}'$ is also inclined. Recovery of salient flow features from active scalars is more challenging, although in this particular case (*f*) there is evidence that the LSM – which entrains relatively warm fluid from the wall, as in the quasi-neutral case (*c*) – subsequently rises due to the coaligned buoyancy force.

Figure 1(*g–i*) shows instantaneous flow visualization results for the limiting flow conditions modelled with LES ($-\zeta_\delta = 266.5$, table 1). For this value of $-\zeta_\delta$, UMZs are now steeply inclined (a prototypical example is visible in (*g*)), as buoyancy has induced far greater vertical mixing. Nevertheless, wedge regions are still visible beneath a series of LSMs. At this limiting $-\zeta_\delta$ value, an ostensible shift from streamwise (mechanical shear) to vertical (thermal flux) dominance has occurred, which is evidenced by visualization of $\tilde{w}$ (*h*) and temperature (*i*). Furthermore, the Obukhov length $|L|$ is very small compared to the height of the structures displayed here (i.e. $|L|/\delta \sim 3.8 \times 10^{-3}$); thus buoyancy is expected to dominate over shear. These results are also consistent with Salesky & Anderson (2018), who reported attenuating amplitude modulation by $\tilde{u}$ with increasing $-\zeta_\delta$. As found previously (for example, Salesky *et al.* 2017), $\tilde{u}'$ and $\tilde{w}'$ fluctuations are out of phase under strong buoyancy forcing, so that low(high)-momentum regions are no longer collocated with regions of relatively warm(cold) fluid. For the limiting inertial conditions addressed in this article, instantaneous visualization poses inherent challenges to recovery of persistent flow features. In order to further the analysis, we below show results from conditional sampling.

Figure 2(*a,c,e,g,i,k*) shows probability density functions (PDFs) of fluctuating streamwise velocity, $\tilde{u}'(\boldsymbol{x}, t) = \tilde{u}(\boldsymbol{x}, t) - \langle \tilde{u}(\boldsymbol{x}, t) \rangle_{xyt}$, where there exists Reynolds- and plane-averaged equivalence under the presumed existence of horizontal statistical homogeneity. Values of the global stability parameter $-\zeta_\delta$ increase from top to bottom (see table 1 for simulation details). The PDFs show thresholds, $\alpha^- = -2\sigma_{\tilde{u}'(\boldsymbol{x}_c, t)/u_\tau}$, which are used when conditionally sampling LMRs from LES output. Figure 2(*b,d,f,h,j,l*) shows the corresponding conditionally sampled streamwise velocity:

$$\frac{\hat{\tilde{u}}'(\boldsymbol{x}, t)}{u_\tau} = \left\langle \frac{\tilde{u}'(\boldsymbol{x}, t)}{u_\tau} \,\middle|\, \frac{\tilde{u}'(\boldsymbol{x}_c, t)}{u_\tau} < -2\frac{\sigma_{\tilde{u}'(\boldsymbol{x}_c)}}{u_\tau} \right\rangle_{N_{\alpha^-}}, \qquad (2.2)$$

where $\boldsymbol{x}_c = \{x, y, 0.05\delta\}$ is the location of the detection criterion and N_{α^-} is the integer number of $\tilde{u}'(\boldsymbol{x}_c, t)/u_\tau < -2\sigma_{\tilde{u}'(\boldsymbol{x}_c)}/u_\tau$ realizations (for example, Antonia 1981). Superimposed upon the $\hat{\tilde{u}}'(\boldsymbol{x}, t)$ colour floods are inclination angles, $\gamma(\zeta_z)$ (solid black, equation (2.1)) and $\gamma_w(\zeta_z)$. The colour flood contours show clear steepening of the conditionally sampled LMRs for increasingly unstable conditions, which previously
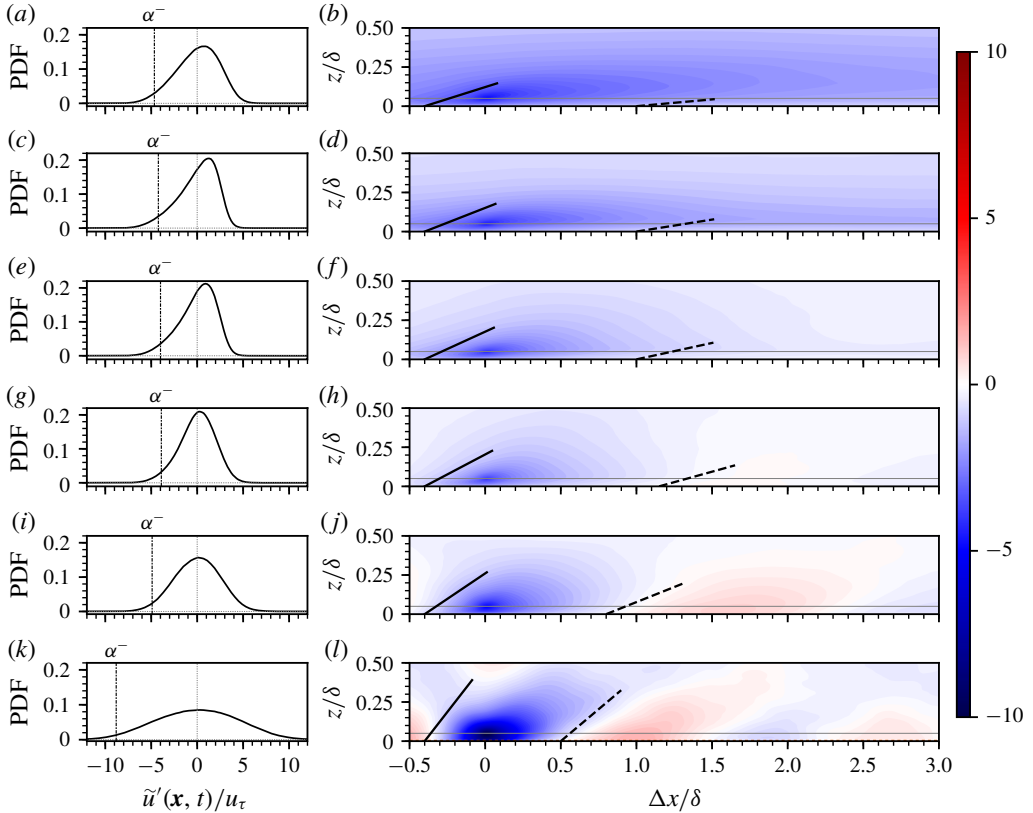
FIGURE 2. Probability density functions of fluctuating streamwise velocity $\widetilde{u}((x),\ t)/u_\tau$ at $z/\delta = 0.05$ (a,c,e,g,i,k) and conditionally averaged streamwise velocity field (b,d,f,h,j,l) $\widetilde{u}'(\boldsymbol{x})/u_\tau$ (2.2) from LES, for stability parameters noted in the legend. Conditional sampling thresholds $\alpha^- = -2\sigma_{\widetilde{u}'(\boldsymbol{x}_c,t)/u_\tau}$ are denoted by the vertical dashed line in (a,c,e,g,i,k). (b,d,f,h,j,l) Streamwise velocity field from LES, conditionally averaged on low-momentum regions $\hat{\widetilde{u}}'(\boldsymbol{x},\ t) = \langle \widetilde{u}'(\boldsymbol{x},\ t)/u_\tau | \widetilde{u}'(\boldsymbol{x}_c,\ t)/u_\tau < -2\sigma_{\widetilde{u}'(\boldsymbol{x}_c)/u_\tau} \rangle$, where $\boldsymbol{x}_c = \{x,\ y,\ 0.05\delta\}$ is the location of the detection criterion (denoted by the horizontal grey line in the velocity field plots). (a,b) $-\zeta_\delta = 0.31$, (c,d) $-\zeta_\delta = 1.81$, (e,f) $-\zeta_\delta = 4.54$, (g,h) $-\zeta_\delta = 9.38$, (i,j) $-\zeta_\delta = 27.9$ and (k,l) $-\zeta_\delta = 266.5$. Solid black lines indicate inclination angles $\gamma(\zeta_z)$ calculated from (3.2) and dashed black lines indicate the angle of the wedge substructure $\gamma_w(\zeta_z) = \gamma(\zeta_z) - \gamma_0$.

has been interpreted as a 'structural thickening' (sketched on the figure 3*a* schematic; see also Salesky & Anderson 2018). However, the present analysis based upon instantaneous flow visualization (figure 1) and conditional sampling (figure 2) offers compelling evidence that the perceived 'inclination' is actually a product of the lower wedge (sketched on the figure 3*b* schematic, which shows the ostensible 'lift up' of the downstream edge of thermally forced LMRs). Results of sampling based upon other quantities are not shown, for brevity, since the resultant scientific deductions are equivalent. Figure 3(*c*) illustrates the inclined LMR, due to the existence of a lower wedge, in agreement with the smoke visualization results provided by Hommema & Adrian (2003) (a theoretical approach for predicting the wedge angle, and thus overall inclination, follows in § 3).
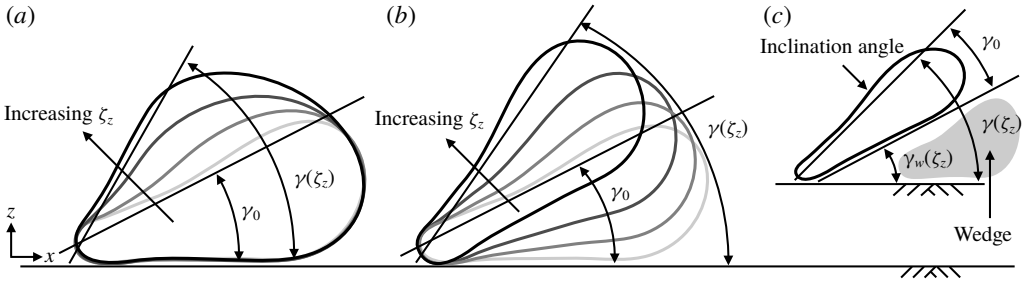
FIGURE 3. Schematic illustrating conceptual interpretation of LSM thickening (*a*), contrasted against results presented in Hommema & Adrian (2003) and herein (*b,c*), wherein LSMs remain notionally self-similar (*b*) but are inclined due to formation of a lower wedge (*c*). Here $\gamma(\zeta_z)$ is the stability-dependent inclination angle, $\gamma_0 = 12°$–$15°$ is the observed inclination angle for neutrally stratified conditions, and $\gamma_w(\zeta_z)$ is the angle of the wedge substructure.

3. Theory

Beginning with arguments set forth in Hommema & Adrian (2003), one can derive a prognostic closure for the inclination angle of LSMs for increasingly unstable thermal stratification, as characterized by the Monin–Obukhov stability parameter ζ_z. The inclination angle γ of an LSM can be written as $\gamma \approx (w/u)$, where u and w are, respectively, the characteristic streamwise and vertical velocity components within an LSM used in this section to denote velocity components). In an unstably stratified flow over a solid boundary, the vertical velocity component can be written as $w = w_p + w_\theta$, where w_p is the vertical velocity due to packet motion and w_θ is vertical velocity due to buoyancy. The inclination angle can then be written as

$$\gamma = \tan^{-1}\left[\frac{w_p}{u} + \frac{w_\theta}{u}\right]. \tag{3.1}$$

In the absence of buoyancy ($w_\theta = 0$), one should recover the inclination angle $\gamma_0 = 12°$–$15°$ observed for neutrally stratified conditions (Carper & Porté-Agel 2004; Marusic & Heuer 2007), which implies that $w_p/u = \tan\gamma_0$. The characteristic streamwise velocity scale can be expressed in terms of the friction velocity, $u = u_\tau$; the vertical velocity due to buoyancy can be expressed in terms of the free convective velocity scale u_f (Wyngaard 2010) – that is, $w_\theta = c_1 u_f = c_1(gzQ_0/\Theta_0)^{1/3}$, where c_1 is a constant (to be determined empirically). Equation (3.1) can then be written as

$$\gamma(\zeta_z) = \tan^{-1}[\tan\gamma_0 + c_1\kappa^{-1/3}(-\zeta_z)^{1/3}] \tag{3.2}$$

$$\approx \gamma_0 + \underbrace{\tan^{-1}[c_2\kappa^{-1/3}(-\zeta_z)^{1/3}]}_{\gamma_w(\zeta_z)}, \tag{3.3}$$

where (3.2) is exact, and (3.3), obtained using the small-angle approximation, allows one to interpret structure inclination angle $\gamma(\zeta_z)$ as the sum of the angle for neutral conditions γ_0 and the stability-dependent inclination of the high-momentum wedge $\gamma_w(\zeta_z)$. Fitting (3.2) and (3.3) to inclination angles calculated from R_{uu} from the AHATS dataset (discussed in §4) with $\gamma_0 = 12°$ yields empirical values of $c_1 = 0.569$ and $c_2 = 0.492$. The approximate equation for $\gamma(\zeta_z)$ (3.3) is within $\sim 1°$ of the exact expression (3.2) for $-\zeta_z \leqslant 1$ and within $\sim 5°$ for $-\zeta_z = 10$.
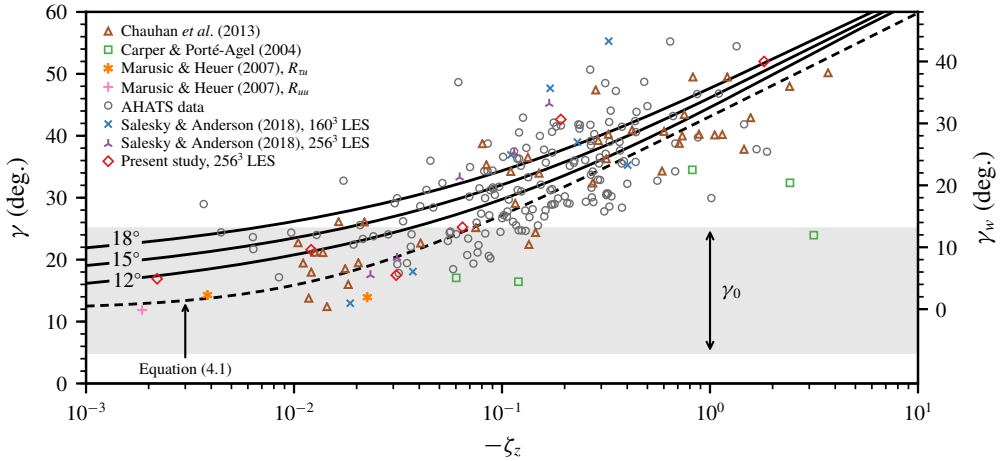
FIGURE 4. Structure inclination angles γ (left ordinate) and corresponding wedge incli-
nation angles γ_w (right ordinate, calculated assuming $\gamma_0 = 12°$) as a function of the MO
stability variable $-\zeta_z$ calculated from the AHATS data and LES for unstable thermal
stratification. Data points are also displayed from the unstable atmospheric surface layer
observations of Carper & Porté-Agel (2004), Chauhan *et al.* (2013) and Marusic & Heuer
(2007), as well as the LES of Salesky & Anderson (2018). The empirical fit from Chauhan
et al. (2013) (4.1) is shown for comparison; the prediction of the prognostic closure (3.2)
is denoted by the solid black lines, plotted for $\gamma_0 = 12°$, $15°$, $18°$. The shaded grey region
indicates the range of inclination angles (γ_0, corresponding to the left ordinate) observed
for neutral stratification (for example, Hommema & Adrian 2003, figure 11(a)).

4. Literature data

Structure inclination angles γ as a function of the stability variable $-\zeta_z$ are
displayed in figure 4 based on published studies using atmospheric surface layer
observations (Carper & Porté-Agel 2004; Marusic & Heuer 2007; Chauhan *et al.*
2013), previous LES results (Salesky & Anderson 2018), the suite of LES runs
detailed in table 1, and additional atmospheric surface layer observations from the
advection horizontal array turbulence study (AHATS) dataset. The observational
studies by Carper & Porté-Agel (2004), Marusic & Heuer (2007) and Chauhan
et al. (2013) were all conducted at the SLTEST facility on the salt flats of western
Utah; structure inclination angles in each study were calculated following the
procedure described in §2, where the two-point correlation of streamwise velocity
$R_{uu}(\Delta x, \Delta z; \zeta_z)$ (2.1) was calculated, and the inclination angle was calculated via
$\gamma = \tan^{-1}(\langle\Delta z/\Delta x^\star\rangle)$. In each case, the stability variable $-\zeta_z$ used for plotting $\gamma(\zeta_z)$
is taken from the reference location (that is, the lowest height used in the calculation
of $R_{uu}(\Delta x, \Delta z)$), consistent with previous studies (Chauhan *et al.* 2013). While
structure inclination angle is a function of z in the general case, the observational
data only allow us to calculate γ for structures in close proximity to the wall.

The AHATS dataset was collected from 25 June to 16 August, 2008 near Kettleman
City, CA, USA. The surrounding terrain was predominantly level and horizontally
homogeneous. We used data from the AHATS profile tower, consisting of Campbell
Scientific CSAT-3 sonic anemometers at $z = 1.51, 3.30, 4.24, 5.53, 7.08$ and 8.05 m,
which sampled the wind velocity vector (u, v, w) and sonic temperature θ at 60 Hz.
The raw 60 Hz data were downsampled to 20 Hz and analysed in 27.3 min blocks,

corresponding to 32 768 data points. Only runs with mean wind angles within $\pm 45°$ of the anemometer axis were included in the analysis, in order to minimize the influence of flow distortion. A coordinate rotation of the raw anemometer data was employed so that the coordinate system was aligned with the mean wind direction (i.e. $\langle v \rangle_t = 0$); standard data quality control criteria were employed to exclude non-stationary blocks from the data analysis (discussed further in Salesky & Chamecki (2012)).

Figure 4 illustrates that the proposed model for LSM inclination angle (3.2), plotted for several values of γ_0 (with $c_1 = 0.569$), is in good agreement with both LES results and field observations across the range of stabilities ($-\zeta_z \in [10^{-3}, 10^1]$) captured by the various datasets. The range of inclination angles γ_0 reported for neutrally stratified conditions (see, for example, figure 11(*a*) of Hommema & Adrian (2003)) is denoted in figure 4 by the grey shaded region. Note that, even in the neutrally stratified case, significant variability has been observed around the typically cited value of $\gamma_0 = 12°-15°$. Also displayed in figure 4 is the empirical fit proposed by Chauhan *et al.* (2013):

$$\gamma(\zeta_z) = 12.0 + 7.3 \ln(1 - 70\zeta_z). \tag{4.1}$$

While both curves capture the observed increase in LSM inclination angles, we note that (4.1) is an empirical fit to the data. Equation (3.2) is based on the theory presented in §3, and captures the observed behaviour of the downstream edge of an LSM lifting up from the wall with the formation of a high-momentum wedge beneath.

5. Conclusions

Observations and numerical simulations of unstably stratified, high-Re_τ, channel turbulence have demonstrated that the inclination angle γ of large-scale motions increases systematically with increasing buoyancy forcing (Hommema & Adrian 2003; Carper & Porté-Agel 2004; Marusic & Heuer 2007; Chauhan *et al.* 2013; Salesky & Anderson 2018) beyond the value $\gamma_0 = 12°-15°$ observed for neutral conditions. However, the effects of unstable thermal stratification on the morphological properties of LSMs, and the connections between LSM structure and observed inclination angles, are not well understood. Some authors have proposed that LSMs incline and thicken while remaining attached to the wall (Salesky & Anderson 2018), while others have suggested that the downstream edge of an LSM lifts away from the wall (Hommema & Adrian 2003) as buoyancy forcing increases.

Using a suite of LES of turbulent channel flow spanning a range of unstable thermal stratification conditions, we use instantaneous flow visualizations and conditional sampling to demonstrate that buoyancy causes the downstream edge of an LSM to lift away from the wall, leaving a wedge of high-momentum fluid beneath, in agreement with the smoke visualizations of Hommema & Adrian (2003). A new prognostic model is developed for LSM inclination angle that accounts for this observed structure; we demonstrate that the inclination angle γ of an LSM can be expressed as the sum of the neutral inclination angle $\gamma_0 \approx 12°$ and the stability-dependent inclination angle of the high-momentum wedge $\gamma_w(\zeta_z)$. Available data from the literature, atmospheric surface layer observations from the AHATS and SLTEST experiments, as well as the LES presented herein, are found to be in good agreement with the prognostic model.

Acknowledgement

Declaration of interests

The authors report no conflict of interest.

Appendix. Large-eddy simulation: numerical procedure, cases

A suite of six LES cases were run in a similar configuration to the LES described in Salesky & Anderson (2018). The simulations were configured to replicate a convective atmospheric boundary layer; the initial condition for the temperature field includes a capping inversion, where the boundary layer depth δ corresponds to the height at which the total heat flux $\langle \widetilde{w}'\widetilde{\theta}' \rangle + \langle q_3^{sgs} \rangle$ attains its most negative value (Salesky & Anderson 2018). The domain size was set to $\{L_x/\delta_0, L_y/\delta_0, L_z/\delta_0\} = \{6, 6, 2\}$ (where $\delta_0 = 1000$ m is the initial boundary layer depth), with a grid resolution of $N_x N_y N_z = 256^3$, corresponding to an LES filter width of $\Delta_x/\delta = \Delta_y/\delta \approx 2.3 \times 10^{-2}$ and $\Delta_z/\delta \approx 7.8 \times 10^{-2}$. The computational domain is sufficient to resolve LSMs for all table 1 cases (Salesky & Anderson 2018), but not VLSMs. However, since VLSMs form via quasi-streamwise coalescence of LSMs, omission of LSMs does not undermine the generality of this article (Hutchins & Marusic 2007); rather, it is preferable to allocate greater spatial resolution to LSMs. The time step was set to $\Delta_t = 0.03$ s. Simulations were run for a total of 480 000 steps, which corresponds to $\sim$17.7 convective turnover times ($T_\ell = \delta/w_\star$) for the least convective ($-\delta/L = 0.31$) case (where $T_\ell = 27\,000\Delta_t$) and $\sim$26.0T_ℓ for the most convective ($-\delta/L$) case (where $T_\ell = 18\,500\Delta_t$). Simulations were forced by a mean horizontal pressure gradient force $-(1/\rho_0)(\mathrm{d}P/\mathrm{d}x)$ with a constant surface heat flux Q_0 (values of forcing parameters can be found in table 1). In contrast to the LES results presented in Salesky & Anderson (2018), the present simulations were run without Coriolis in order to ensure that LSMs were aligned with the *x*-coordinate axis at all heights for flow visualization purposes. All other initial and boundary conditions are identical to those presented in Salesky & Anderson (2018). Note that the present simulations have higher spatial resolution than the highest-resolution cases presented in Salesky & Anderson (2018); thus sensitivity to the numerical grid employed is expected to be minimal (grid invariance has been previously established and presented in the appendix of Salesky *et al.* (2017)). The forcing used for each simulation, boundary layer depth δ, Obukhov length L, friction velocity u_τ, bulk stability parameter $\zeta_\delta = -\delta/L$, and Deardorff convective velocity scale $w_\star = (g\delta Q_0/\Theta_0)^{1/3}$ (where g is gravity and Θ_0 is a reference potential temperature at the surface) can be found in table 1.

$-\rho_0^{-1}(\mathrm{d}P/\mathrm{d}x)$ (m s^{-2})	Q_0 (K m s^{-1})	δ (m)	$\|L\|$ (m)	$\zeta_\delta = -\delta/L$ (—)	u_τ (m s^{-1})	$w_\star$ (m s^{-1})
1.5×10^{-3}	0.07	1094	3570	0.31	1.48	1.35
1.1×10^{-3}	0.24	1172	649	1.81	1.27	2.08
7.0×10^{-4}	0.24	1148	253	4.54	0.93	2.07
5.0×10^{-4}	0.24	1141	121.5	9.38	0.73	2.07
3.0×10^{-4}	0.24	1141	40.9	27.9	0.50	2.07
1.0×10^{-4}	0.24	1148	4.31	266.5	0.24	2.07

TABLE 1. Properties of LES cases: mean pressure gradient force, $-\rho_0^{-1}(\mathrm{d}P/\mathrm{d}x)$; kinematic surface heat flux, Q_0; flow depth, δ; Obukhov length, L; global stability parameter, $\zeta_\delta = -\delta/L$; friction velocity, u_τ; and Deardorff convective velocity scale, $w_\star$.

References

ANTONIA, R. A. 1981 Conditional sampling in turbulence measurement. *Annu. Rev. Fluid Mech.* **13**, 131–156.

CARPER, M. A. & PORTÉ-AGEL, F. 2004 The role of coherent structures in subfilter-scale dissipation of turbulence measured in the atmospheric surface layer. *J. Turbul.* **5**, 32–32.

CHAUHAN, K., HUTCHINS, N., MONTY, J. & MARUSIC, I. 2013 Structure inclination angles in the convective atmospheric surface layer. *Boundary-Layer Meteorol.* **147** (1), 41–50.

DESHPANDE, R., MONTY, J. P. & MARUSIC, I. 2019 Streamwise inclination angle of large wall-attached structures in turbulent boundary layers. *J. Fluid Mech.* **877**, R4.

FAN, D., XU, J., YAO, M. X. & HICKEY, J.-P. 2019 On the detection of internal interfacial layers in turbulent flows. *J. Fluid Mech.* **872**, 198–217.

HOMMEMA, S. E. & ADRIAN, R. J. 2003 Packet structure of surface eddies in the atmospheric boundary layer. *Boundary-Layer Meteorol.* **106** (1), 147–170.

HUTCHINS, N. & MARUSIC, I. 2007 Evidence of very long meandering features in the logarithmic region of turbulent boundary layers. *J. Fluid Mech.* **579**, 1–28.

MARUSIC, I. & HEUER, W. D. C. 2007 Reynolds number invariance of the structure inclination angle in wall turbulence. *Phys. Rev. Lett.* **99** (11), 114504.

SALESKY, S. T. & ANDERSON, W. 2018 Buoyancy effects on large-scale motions in convective atmospheric boundary layers: implications for modulation of near-wall processes. *J. Fluid Mech.* **856**, 135–168.

SALESKY, S. T. & CHAMECKI, M. 2012 Random errors in turbulence measurements in the atmospheric surface layer: implications for Monin–Obukhov similarity theory. *J. Atmos. Sci.* **69** (12), 3700–3714.

SALESKY, S. T., CHAMECKI, M. & BOU-ZEID, E. 2017 On the nature of the transition between roll and cellular organization in the convective boundary layer. *Boundary-Layer Meteorol.* **163** (1), 41–68.

WYNGAARD, J. C. 2010 *Turbulence in the Atmosphere*. Cambridge University Press.